GEOMETRIC ROUGHNESS EFFECTS ON THE AERODYNAMIC CHARACTERISTICS OF A SPINNING CYLINDER IN CROSSFLOW

Simon Prince, Jenny Holt & Petros Episkopou
School of Aerospace, Transport and Manufacturing, Cranfield University, UK.

Abstract

An experimental study is presented, assessing the effect of different configurations of relatively large scale geometric surface roughness on the aerodynamic performance of a spinning cylinder in crossflow. The characteristics of the baseline smooth surface spinning cylinder were measured and analyzed using computational fluid dynamics, before the roughness configurations were experimentally assessed.

Spanwise ribs, crossing the entire length of the cylinder with no gaps, have been found to be significantly more effective in augmenting spinning cylinder lift, with higher lift to drag ratio, than employing streamwise ribs or large scale geometric roughness elements – in this case diamond protuberances.

1 Introduction

The high level of lifting force that can be generated by the Magnus effect, via a spinning cylinder in crossflow, has been the impetus for many studies into how this effect may be utilized. These have included propulsive force generation, as in the case of the Flettner rotor ships, the generation of high lift for wings, and for boundary layer control.

While spinning cylinders are capable of generating much higher lifting forces, per unit span, than more conventional lift configurations, such as the flapped wing, the drag force is also considerably higher. The application of surface roughness to reduce the drag of static cylinders, by forced transition of the surface boundary layer resulting in more rearward separation and a much reduced wake extent, is well known.

This paper reports on an experimental and computational study of the effect of surface roughness configurations on the aerodynamic performance of a spinning cylinder, data on which is sparse in the literature.

2. The Aerodynamics of Spinning Cylinders.
2.1 The Magnus and Inverse Magnus Effect.

Benjamin Robins [1] reported in 1742 that artillery shells tended to depart from ballistic trajectories when spinning about their longitudinal axis. Gustav Magnus [2], however, is credited with the discovery, in 1853, that a rotating cylinder in crossflow experiences a force at right angles to the crossflow direction. In particular he identified that this "Magnus" force occurs in the direction towards the side where the peripheral surface velocity is in the same direction as the freestream velocity.

This "Magnus effect" was first explained as resulting from induced circulation by Lord Rayleigh [3] in 1877, and by the early 20th Century much experimental work was being done to assess the practical viability of using the spinning cylinder Magnus force.

Ludwig Prandtl [4] first experimented with spinning cylinders in 1906, and realized the critical importance that the boundary layer had in the generation of the Magnus force. Lafay [5] discovered that the Magnus side force could, under certain conditions, reverse in direction to that opposite to that reported by Magnus. Later work experimental work by Thom [6 - 9] Krahn [10], Kelly and Van Aken [11] and Swanson [12] provided the physical explanation for this "Inverse Magnus" effect.

Figure 1 depicts the typical flow structure for the crossflow around a spinning cylinder. The action of the surface rotation displaces the origin of the boundary layer and the locations of

the separations on the upper and lower sides of the cylinder. The physics of this flow is highly sensitive to the Reynolds number, Re_D, of the flow, and the surface rotational to freestream speed ratio, Ω, both of which dictate the state of the boundary layer, the separated shear layer and the downstream wake.
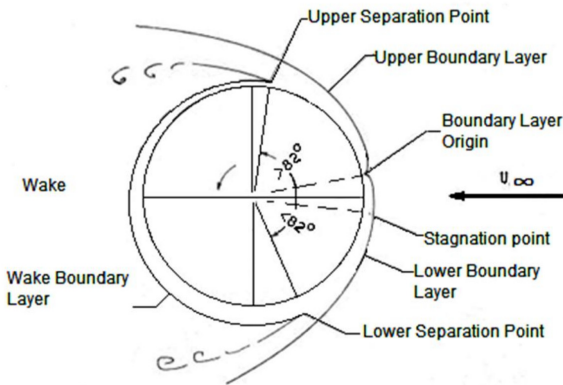

Fig. 1: Schematic representation of the viscous crossflow around a spinning cylinder [12]

The physics of the different flow regimes for spinning cylinders in crossflow, can be classified in the same manner as the crossflow about a static cylinder. Table 1 presents the different physical regimes of flow, their designation, and the associated range of Reynolds number.

State		Regime		Re_D range
L	Laminar	1	No-separation	0 to 4–5
		2	Closed wake	4–5 to 30-48
		3	Periodic wake	30-48 to 180-200
TrW	Transition in wake	1	Far-wake	180-200 to 220-250
		2	Near-wake	220-250 to 350-400
$TrSL$	Transition in shear layers	1	Lower	350-400 to 1k–2k
		2	Intermediate	1k-2k to 20k-40k
		3	Upper	20k-40k to 100k-200k
$TrBL$	Transition in boundary layer	0	Pre-critical	100k-200k to 300k-340k
		1	Single-bubble	300k-340k to 380k-400k
		2	Two-bubble	380k-400k to 500k - 1M
		3	Supercritical	500k-1M to 3.5M - 6M
		4	Post-critical	3.5M – 6M to ?
T	Fully turbulent	1	Invariable	? to ∞
		2	Ultimate	

Table 1: Typical flow states encountered around static cylinders in crossflow [13].

At very low Reynolds numbers the boundary layer is laminar on both sides of the cylinder (the L state). Transition will first occur in the far wake and will occur close in to the cylinder with increasing Re_D (TrW state) until transition begins in the shear layers just off the cylinder surface ($TrSL$ state). With further increase in

Re_D, transition will move into the cylinder boundary layers ($TrBL$ state) and the effected boundary layers, suitably energized, will separate from a much more rearward location. The surface rotation will result in the boundary layer on the side of the cylinder where the surface rotates with the freestream flow, transitioning first. This will result in a much greater extent of attached flow, and surface suction on this side. The resulting asymmetry in suction gives rise to the inversion in the Magnus force. As Re_D increases further, there will come a point where both sides of the cylinder have turbulent separations (T state), and normal Magnus effect behavior will recover. Figure 2 presents, for a static cylinder in crossflow, the typical variation of C_L and C_D with Re_D as the boundary layer, shear layer and wake states change. A spinning cylinder, at a constant spinning speed, will behave in a similar manner with variation in Reynolds number.
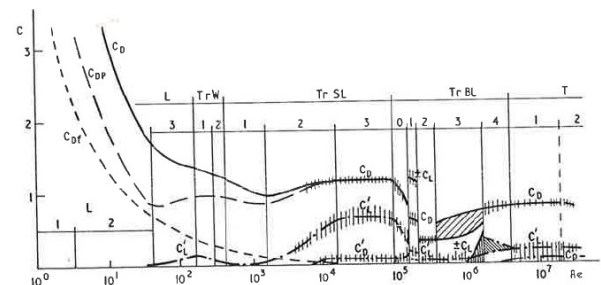

Fig. 2: Typical variation time averaged C_D and C_L with Reynolds number for static cylinders in crossflow [13]

2.2 The Effect of Surface Roughness

The effect of surface roughness on the flow around non-spinning cylinders is well known, and understood. Surface roughness will have the effect of promoting premature transition of the boundary layers, and an earlier reduction of C_D associated with the narrowing of the wake. For a fully turbulent flow, the introduction of surface roughness tends to increase the surface skin friction of the attached boundary layers, and thereby increase the level of C_D for a given Re_D. The shedding frequency is also known to be effected by surface roughness in all flow regimes. These trends are comprehensively reviewed by Zdravkovich [13].

Very few studies have been undertaken on the effect of surface roughness on the flow around a spinning cylinder, however. Thom [7, 9] examined the effect of sand roughness (no size specified) on a cylinder of Aspect-Ratio, $AR = 8.1$, in the range $5k < Re_D < 12.5k$, which is in the *TrSL2* state. Figure 3 presents Thom's results for C_L and C_D and shows very little effect until spinning at Ω of ~3 and above, when the roughness is seen to have suppressed the lift plateau to high spinning speed. It is thought that the stable laminar state of the cylinder boundary layers explains the lack of effect at the lower spinning speeds.
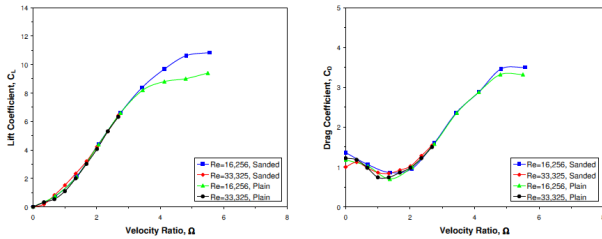
Fig. 3: The effect of distributed surface roughness on a spinning cylinder. Results of Thom [7, 9].

Takayama & Aoki [14] investigated the effect of circular grooves on a spinning cylinder, the geometric details of which are reproduced in figure 4. Tests were performed on the model of $AR=2.15$, having end plates of diameter to cylinder diameter ratio, $D_e/D = 1.375$, in the range $40k < Re_D < 180k$, which is in the *TrSL3 / TrBL0* regime.
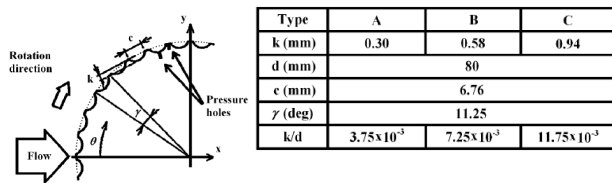

Fig. 4: The grooved cylinder geometries of Takayama & Aoki [14]

Figure 5 presents the variation of lift C_L with Ω for the smooth cylinder and the three roughness geometries of Takayama & Aoki at the seven Reynolds numbers tested. Figure 6 presents the corresponding data for C_D. It was found that an inverse Magnus force was generated with the smooth cylinder for $Re_D >$

1.0×10^5 but the effect of the cylinder grooves was to suppress the inverse Magnus effect for all Reynolds numbers above 40k. As the groove depth was increased, the lift curve slope was found to reduce. In addition, as the groove depth was increased the drag coefficient became effectively independent of the spinning rate. These phenomena were all associated, through observation using the spark tracing flow visualization technique, with boundary layer transition and the movement of the separation locations.
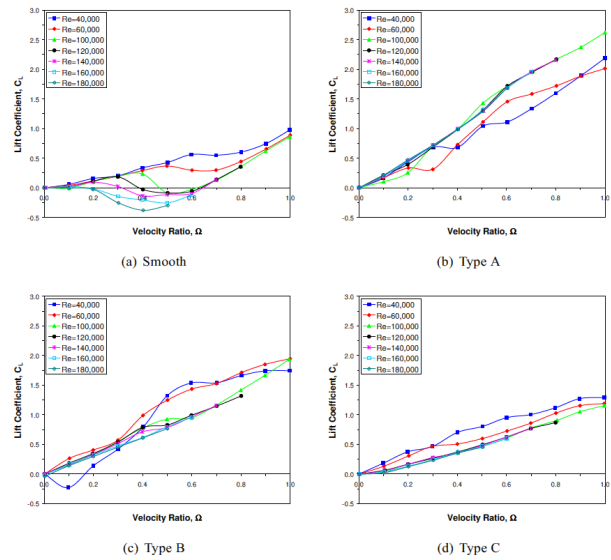

Fig. 5: The effect of spanwise grooves on the lift coefficient of a spinning cylinder. Results of Takayama & Aoki [14].
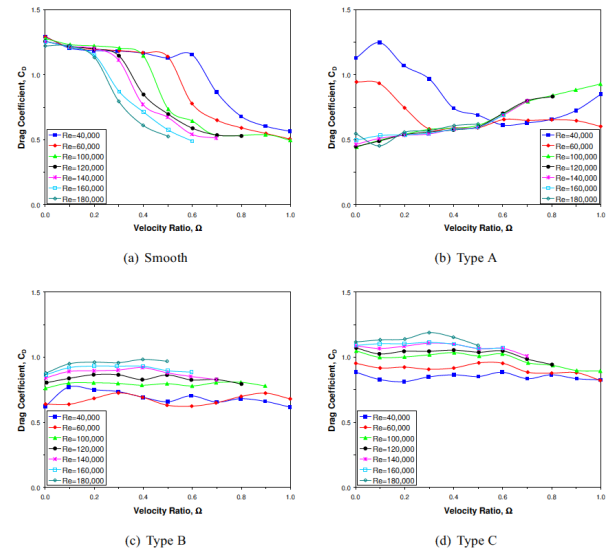

Fig. 6: The effect of spanwise grooves on the drag coefficient of a spinning cylinder. Results of Takayama & Aoki [14].

3 Investigation Methodology

3.1 The Experimental Tests

The spinning cylinder configurations under investigation here, are based on the smooth surface cylinder tested by Badalanenti et al [15 – 17]. This was an aluminium cylinder of 88.9mm diameter with co-spinning end plates twice this cylinder diameter, as shown in figure 7a. The aspect ratio of the cylinder was 5.1. The cylinder was mounted to a turntable on the wind tunnel working section floor, by means of two identical streamlined struts connected to the central spindle of the cylinder model, as shown in figure 8. The motor which drove the cylinder was a Graupner Ultra 3300-7 variable speed DC electric motor mounted to the side of one of the struts. To maintain symmetry of shape, a 'dummy motor' of approximately the same size and weight as the motor, was attached to the strut on the other side of the cylinder. Full details of the model design are provided in reference [15]. Three other cylinder models, each incorporating different large scale roughness configurations, were manufactured to make use of the same end-plates and mounting assembly. Details of the roughness geometries are presented in figure 7.
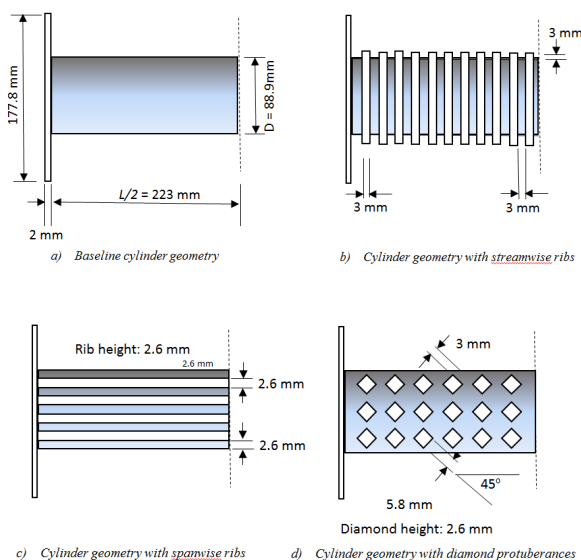

a)   Baseline cylinder geometry   *b)   Cylinder geometry with streamwise ribs*

c)   Cylinder geometry with spanwise ribs   *d)   Cylinder geometry with diamond protuberances*

Fig. 7: The cylinder geometries

The struts penetrated the floor turntable and are connected to an underfloor balance arrangement. The force balance consisted of two JR3 Inc 45E15A4-I63-AF load balances (2000 Hz acquisition rate), one for each strut, such that the total lift (vertical) force and drag (horizontal) forces were given by the addition of the two measured components. Power was supplied to the motor by two type 063, lead-acid 12V batteries. The use of a battery rather than a DC power-pack allowed the implementation of high rotation rates where current draw was in excess of 10A. Variation of the cylinder rpm was achieved by placing a 6.35 ohm rheostat in series with the motor.
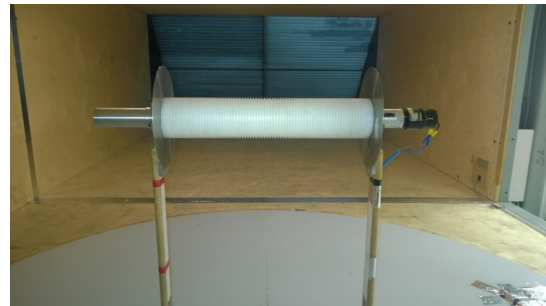

Fig. 8: The spanwise ribbed cylinder mounted in the Cranfield 8ft x4ft Low Speed Wind Tunnel.

Measurements were made in the Cranfield University Atmospheric Boundary-Layer Wind Tunnel which has a rectangular working section of 8ft x 4ft and is vented to atmosphere at the rear. The facility has an air speed range of 0.5m/s – 16m/s, and has low turbulence (<1%) characteristics. Freestream air speed was measured via a pitot-static tube arrangement carefully mounted downstream of the working section to avoid disturbance, and connected to a piezo-electric differential pressure transducer. A laser optical tachometer sensor, together with reflective strips mounted onto one of the end plates, was used to record cylinder rpm.

Wind speed, cylinder rpm and balance forces were fed into a NI PCI 6251, and the channels processed through a LabView program to provide synchronized data, logged at a rate of 2000Hz.

Corrections due to tunnel blockage were not made in this study as the area blockage was calculated as being only 1.8%. All measured forces were corrected for model weight, and wind-on measurements were taken, across the wind speed range, for the lift and drag contributions of the assembly without a central

cylinder. These tare measurements were then removed from the measurements in the cylinder tests in order to resolve the cylinder-only contribution.

3.2 The Computational Simulations

In addition to the experimental study a CFD analysis was performed to assess the ability of modern unsteady Navier-Stokes simulations to resolve the physical trends associated with spinning cylinders in crossflow in these relatively high Reynolds number flows. In this study both the cylinder itself, and the end plate were modelled in an attempt to resolve the correct aspect ratio effect, including the roll up of the vortex formed from the end plates, and their effect on the vortex shedding in between.

For this analysis the FLUENT flow solver was employed to computed the half-model unsteady flow, where a symmetry plane was enforced on the x-z plane at y=0, as shown in figure 9. Structured multiblock grids were generated, as shown in figure 9 which depicts the intermediate cell density mesh.
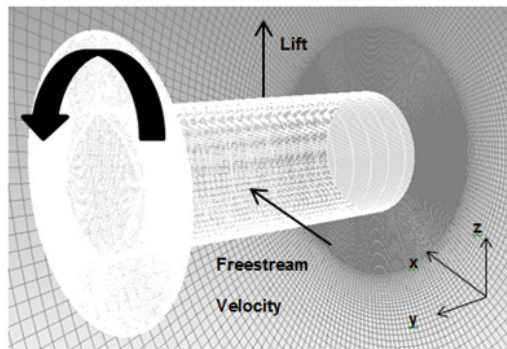

Fig. 9: 3D structured surface mesh and symmetry plane mesh for the smooth surface spinning cylinder with end plate.

Boundary layer cell clustering was employed on all wall surface, where the first cell height was set as $1.0 \times 10^5 D$ in all cases. The flow explicit time-marching Navier-Stokes solver was employed with the third-order MUSCL special scheme. Since calculations were performed at a constant freestream speed on 10m/s, the Reynolds number, Re_D=5.7x10^5, suggests the flow is quite firmly in the *TrSL3* regime, meaning that the simulations were all run in laminar flow mode, and no inverse

Magnus effect would therefore be expected. Time-steps of 0.002 seconds were employed with 20 iterations per time step.

Three grids were tested for the no-spin case, these having ~1.35million, ~1.72million and ~2million cells respectively. Since the intermediate and fine cell density grid gave the same drag force and Strouhal shedding frequency to within 2 significant figures, the fine 2million cell grid was employed for the spinning cases.

4 Results

4.1 Smooth Cylinder Characteristics

Figure 1 presents the comparison between the aerodynamic characteristics for the smooth cylinder measured in the present study with those at similar Re_D measured by Badalamenti. The agreement is seen to be remarkably good for both lift and drag, with Reynolds number effects only becoming significant at low and very high spinning rates.

a) C_L versus Ω
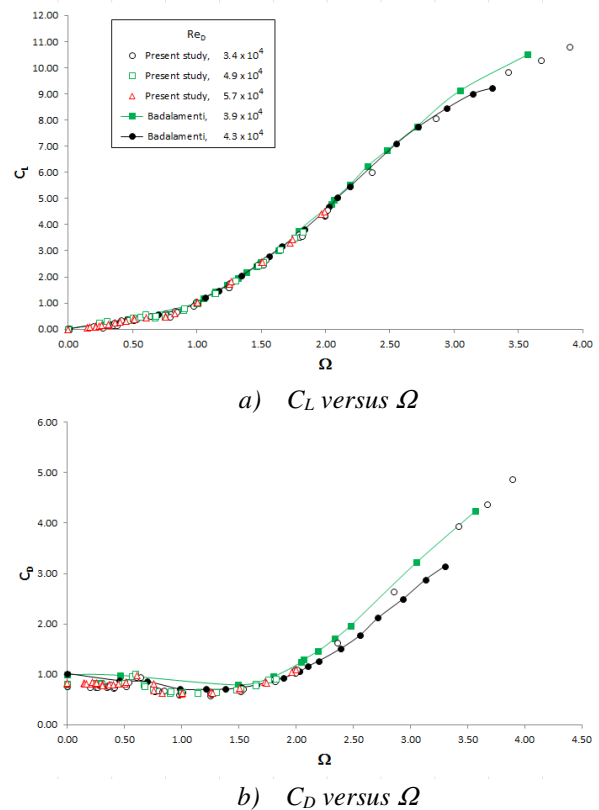

b) C_D versus Ω

Fig. 10: The aerodynamic characteristics of the smooth surface spinning cylinder. Comparison of the present measurements with those of Badalamenti [5].

A comparison of the lift variation with Ω at the lower spinning speeds, between the present measurements and those of Swanson, are plotted in figure 11. The agreement between the two datasets is seen to be reasonably good, despite the excessive scatter in the present data, which is predominantly a result of excessive structural vibration at the lower spinning speeds, rather than measurement inaccuracy. Here the inverse Magnus effect is clearly evident in the Swanson data. The present data, for all three Reynolds numbers, indicate a shallowing off of the lift gradient at around $0.4 < \Omega < 0.7$, which is indicative of an inverse Magnus event, consistent with the trends in the Swanson data. This is better seen in the plot of figure 12a).
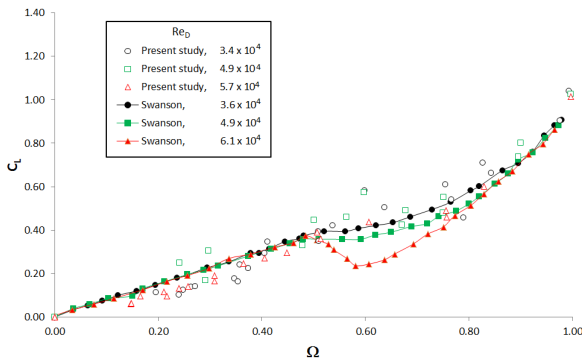

Fig. 11: Variation of C_L with Ω indicating the Magnus effect. Comparison of the present measurements with those of Swanson [12].

Figure 12a) plots only the present C_L data and demonstrates that at the higher spinning speeds, where the structural vibration of the model appeared to be suppressed, the lift curves for all the Reynolds numbers were effectively equivalent, within the limits of measurement accuracy. The inverse Magnus trends in the present data are more obvious in this plot, and seem to be associated with a significant "hump" in the drag trend with Ω, seen in figure 12b). This was not observed in the data of Badalamenti. The measurements of Swanson, plotted in this figure, and others suggest that C_D for the static cylinder should be at the fully laminar level of around 1.2 in the subcritical Reynolds number range tested here, whereas the measured result in this study, of around 0.8, is closer to that expected of a post-critical flow,

with turbulent boundary layer separation. It is suggested that the model vibration for $\Omega < 0.6$, which was observed in the wind tunnel, effectively tripped the flow into the *TrBL0* state where a significant extent of the cylinder boundary layer, though not all, was turbulent. The subsequent suppression of structural vibration at the higher spinning speeds possibly resulted in a re-laminarisation and subsequent boundary layer transition which resulted in the inverse Magnus trend seen in the lift data.
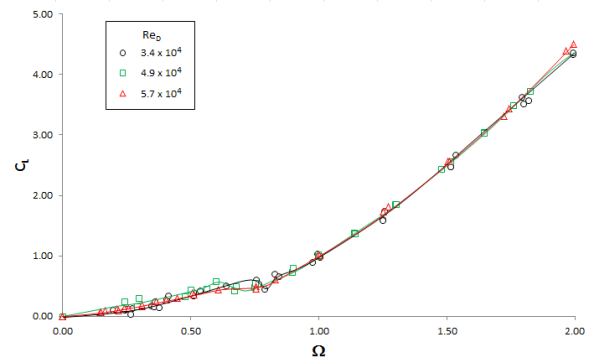
a) C_L versus Ω
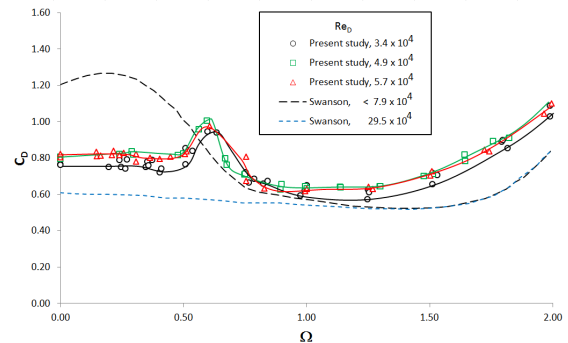
b) C_D versus Ω

Fig. 12: Detailed comparison of the aerodynamic characteristics of the smooth surface spinning cylinder for the 3 Reynolds numbers tested in the present study.

Shedding Strouhal number, St, was acquired via fast Fourier transform analysis, using the Hanning windowing function for a block size of 2048, of the unsteady C_L data. The variation of St with Ω is presented in figure 13 with comparisons with past data. The present results exhibit the same trends as that of the past data, with St levels of around $0.14 - 0.18$ for the static cylinder, rising up to a level of around $0.24 - 0.28$ for Ω of 1.4. Beyond this spinning speed it was difficult to resolve the shedding signal in the present data, as the known

shedding suppression effect took hold. The results are in good agreement with past data, within the accuracy of the measurements and the data processing routines, which were not deemed to be accurate enough to resolve any Reynolds number sensitivity.
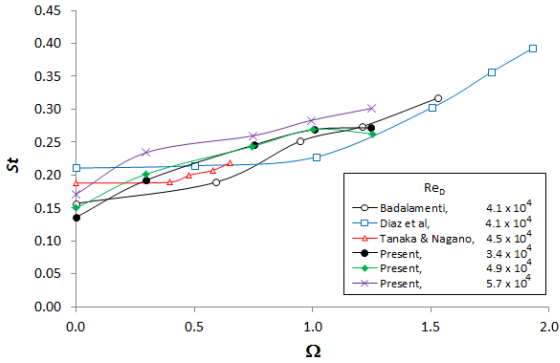

Fig. 13: Comparison of the computed shedding Strouhal number versus Ω for the smooth surface spinning cylinder.

The variation of the computationally predicted forces and shedding Strouhal number, with Ω, are compared with measurements in figure 14 for the 10/s freestream case. The agreement between CFD, which assumes laminar boundary layer state across the whole Ω range, and the experimental data for C_L is remarkably good. It is important to note that laminar CFD would not have been expected to resolve any inverse Magnus effect. The drag predictions provide C_D levels for the purely laminar laminar flow computed, to be about $\Delta C_D \sim 0.1$ below the measured levels at low spinning speeds. This is consistent with the suggestion that the structural vibration in the experiment resulted in some boundary layer transition in the experimental flow. The CFD resolved shedding Strouhal number, obtained using the same FFT algorithm, of the computed fluctuating lift data is seen to be in reasonable agreement with the experimentally measured figures.

The agreement between the CFD predictions and the measured data provides some confidence that the simulated physical flow fields and the resolved trends with cylinder spinning speed are likely to be faithfully resolved, except for the effect of boundary layer transition which is not resolved in the CFD.
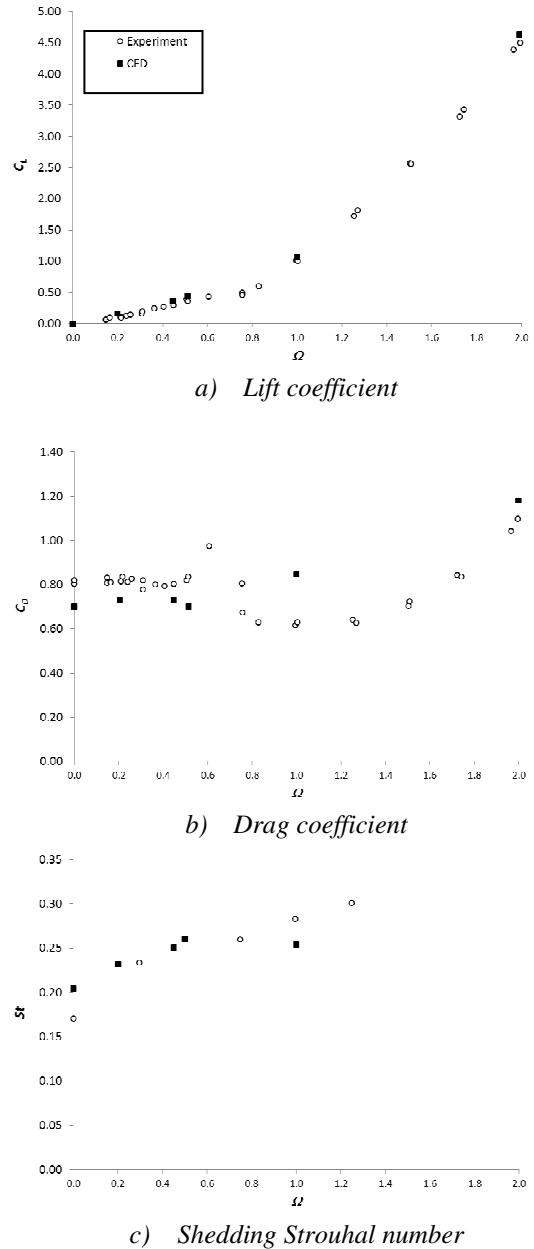

a) Lift coefficient

b) Drag coefficient

c) Shedding Strouhal number

Fig. 14: Comparison of the experimental and CFD predicted force and wake shedding characteristics versus Ω for the smooth surface spinning cylinder, U=10m/s, $Re_D = 5.7 \times 10^4$.

Figure 15 presents contours of computed instantaneous velocity magnitude in the symmetry plane, for Ω of 0, 1.0 and 2.0 for the $C_{L(max)}$ and $C_{L(min)}$ conditions for the 10m/s freestream flow case. For Ω=0 there is an extensive separated, low velocity, wake with primary vortex shed alternately from the upper and lower surface. At Ω=1.0 the minimum velocity levels in the wake are seen to be increased, while a significant downward deflection of the wake is observed for the $C_{L(max)}$ condition. In addition the extent of accelerated

flow around the sides of the cylinder is seen to have increased, particularly in downstream extent.
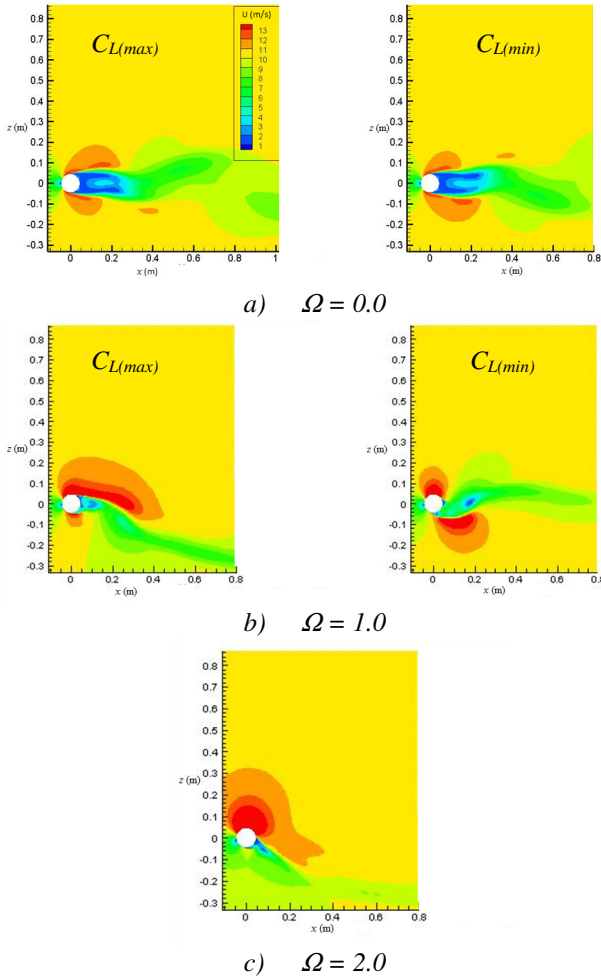

a) $\Omega = 0.0$

b) $\Omega = 1.0$

c) $\Omega = 2.0$

Fig. 15: Sample contours of computed instantaneous velocity on the cylinder symmetry plane. Smooth surface, U = 10m/s, $Re_D = 5.7x10^4$.

By Ω=2.0 the unsteadiness in the CFD predicted flowfield was drastically reduced so that flowfield remained relatively constant as depicted in figure 15c), with a nearly constant downward deflection of the wake of around 40° angle, and a considerable region of highly accelerated flow over the upper cylinder surface, which results in very high surface suctions and corresponding lift force. This suppression of eddy shedding into the wake at the spinning speed approaches Ω=2.0 is reported in the literature [13, 15, 16, 17].

In summary modern CFD seems capable of resolving the large scale physics of spinning cylinder flow, including the Magnus effect.

However, it is suggested that there remain serious challenges in the prediction of flows where boundary layer transition is important (inverse Magnus effect), and where the effect of turbulence requires the solution via more complex methods such as Detached Eddy Simulation or Large Eddy Simulation.

4.2 The Effect of Surface Roughness

The smooth surface experiments, which were repeated three times for each Reynolds number, were performed again, three times, for each of the three roughness configurations. Figure 16 presents the force characteristics of three of the surface configurations for a freestream flow of 6m/s (Re_D=3.4x10^4) - the data for the streamwise rib configuration at the condition was not available at the time of writing. Figure 17 presents the corresponding data for a 10m/s freestream (Re_D=5.7x10^4), which includes data for all four roughness configurations.

At the lower Reynolds number the lifting characteristics of the cylinder with diamond protuberances was found to be very close to the smooth surface cylinder, but with no inflexions due to boundary layer transition effects. The drag characteristic with the diamond protuberances follows the same trend as the post-critical behavior measured by Swanson and shown in figure 12, which supports the view that the flow is almost certainly fully turbulent in this case, which would explain why no inflexions appear in the lift curve.

This would also support the suggestion that the hump in the drag curve for the smooth cylinder, which does not appear in any of the curves with roughened surface, is association with an initially turbulent boundary layer (due to structural vibration at low spinning speeds) turning laminar as the vibration disappears at higher spinning speeds, and then subsequently transitioning at the expected point around Ω=0.6.

Interestingly the spanwise ribs are seen to considerably increase the Magnus lift for Ω > 0.7, with almost twice the C_L level at Ω=1.0. The drag characteristic also follows a typical post-critical trend but the drag rise, in this case, occurs earlier with spanwise ribs than with

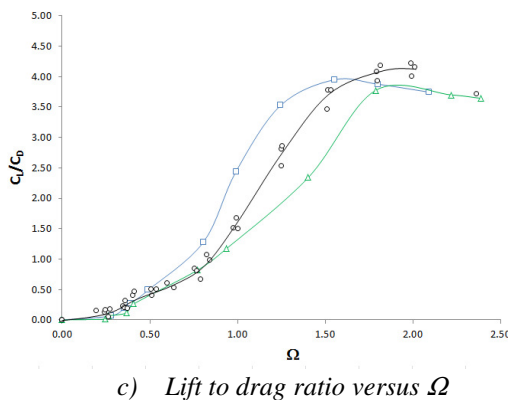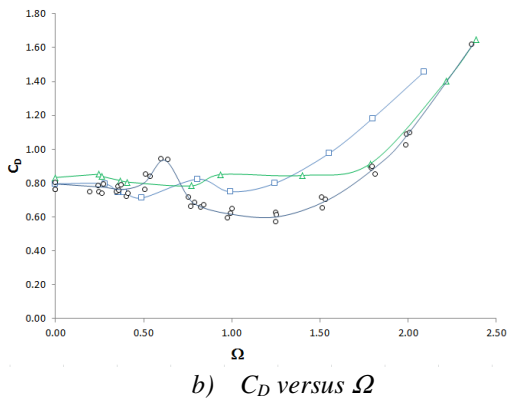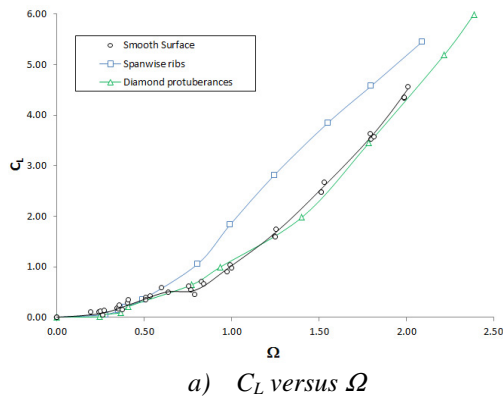diamond protuberances – possibly due to increased induced drag effect.

a) C_L versus Ω

b) C_D versus Ω

c)   Lift to drag ratio versus Ω

Fig. 16: Comparison of the effect of the different surface roughness configurations on the aerodynamic characteristics of the spinning cylinder. U=6m/s. Re_D=3.4x10⁴.

The lift to drag ratio, plotted in figure 16c) shows that the spanwise ribbed cylinder outperforms the smooth cylinder, in terms of efficient lift generation, by a considerable margin in the range 0.6 > Ω > 1.6, whereas the diamond protuberances have a negative impact for all but the lowest spinning speeds.

Figure 17 presents the corresponding data for a 10m/s freestream and shows that these trends

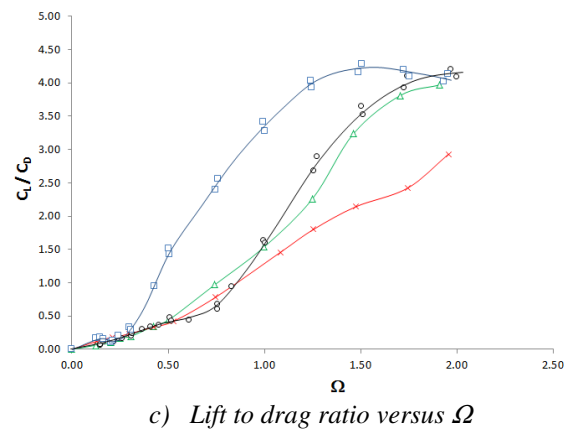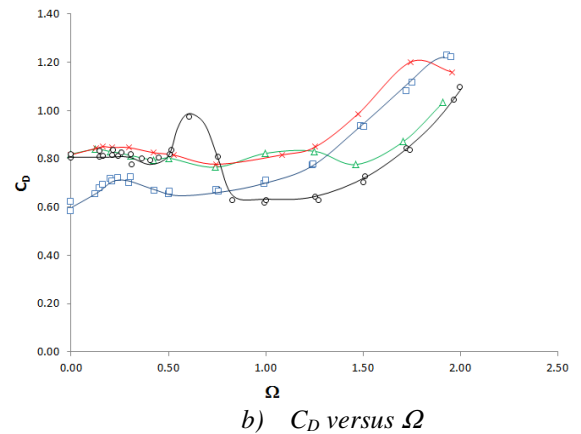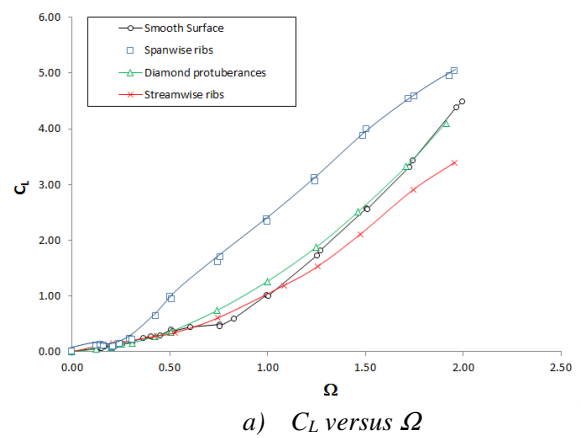are also observed at this higher Reynolds number.

a) C_L versus Ω

b) C_D versus Ω

c)   Lift to drag ratio versus Ω

Fig. 17: Comparison of the effect of the different surface roughness configurations on the aerodynamic characteristics of the spinning cylinder. U=10m/s. Re_D=5.7x10⁴.

The lift augmentation due to spanwise ribs is even more marked in this case, and the drag level at the lowest spinning speeds is as expected of a fully turbulent cylinder flow, which is considerably lower that for the other three surface configurations. The effect of streamwise ribs, at this Reynold number, was

found to be a slightly reduced lift, compared with the smooth surface case, at the higher spinning speeds, while the drag curve follows that for the diamond protuberances before a drag rise begins earlier at Ω ~1.2. Overall the spanwise ribs are seen to be the clear winner in delivering the most efficient Magnus lift effect, while the streamwise ribs appear to be the worst.

Figure 18 presents the effect of the different roughness configurations on the measured shedding Strouhal number. The addition of large scale geometric roughness was not found to alter the general trend of an increase in St with Ω, where shedding into the wake is suppressed at the higher spinning speeds. Measurement uncertainty and that associated with the FFT processing does not allow assessment of the effect on relative magnitude of St.
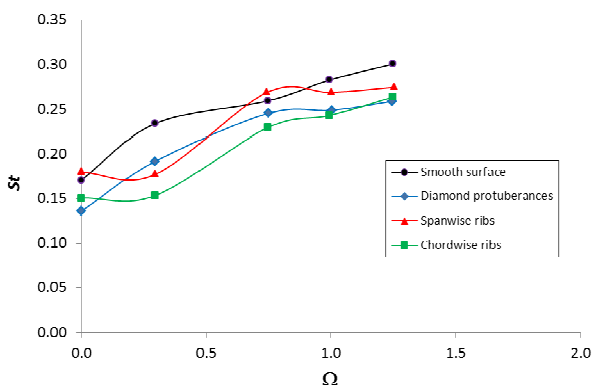

Fig. 18: Comparison of the effect of the different surface roughness configurations on the measured Strouhal number. U=10m/s. Re_D=5.7x10^4.

The physical origin of these roughness effects is presently unclear – and will need to be further investigated via experiment, which is the aim of a follow on study.

5 Conclusions

Spanwise ribs, crossing the entire length of the cylinder with no gaps, have been found to be significantly more effective in augmenting spinning cylinder lift, with higher lift to drag ratio, than employing streamwise ribs (disc like appendages) or large scale geometric roughness elements – in this case diamond protuberances.

References

[1] Robins, B. "New Principles of Gunnery" London 1742.

[2] Magnus, G., "On the Deflection of a Projectile", *Poggendorf's Annalen der Physik und Chemie*, Vol. 88, 1853, pp604-610.

[3] Lord Rayliegh, "On the Irregular Flight of a Tennis Ball", *Messenger of Mathematics*, Vol. 7, pp 14–16.

[4] Prandtl, L. & Tietjens, O., "Applied Hydro-and Aeromechanics", MacGraw-Hill Book Company, Inc., New York, NY, 1961, pp. 80–85.

[5] Lafay, A., "On the Inversion of Magnus Phenomena", *Compt. Rend/ Acad. Sci.*, Vol. 151, No. 61, 1910.

[6] A. Thom, "The Aerodynamics of a Rotating Cylinder", Ph.D. thesis, University of Glasgow, UK, 1926.

[7] A. Thom, "Experiments on the Air Forces on Rotating Cylinders", Technical Report R&M No. 1018, Aeronautical Research Council, 1925.

[8] A. Thom, "Experiments on the Flow Past a Rotating Cylinder", Technical Report R&M No. 1410, Aeronautical Research Council, 1931.

[9] A. Thom, "On the Effect of Discs on the Air Forces on a Rotating Cylinder" Technical Report R&M No. 1623, Aeronautical Research Council, 1934.

[10] Krahn, E., "Negative Magnus Force", *J. Aero. Sci.,* Vol 23, pp 377-8.

[11] Kelly, H. R. and Van Aken, R. W., "The Magnus Effect at High Reynolds numbers", *J. Aero. Sci.*, Vol. 23, pp 1053-4.

[12] W. M. Swanson, "The Magnus Effect: A Summary of Investigations to Date", *Journal of Basic Engineering*, Vol. 83, 1961, pp. 461–470.

[13] Zdravkovich, M. M., "Flow Around Circular Cylinders" Vol. 1: Fundamentals, and Vol. 2: Applications, Oxford University Press, 2003.

[14] S. Takayama and K. Aoki, "Flow Characteristics around a Rotating Grooved Circular Cylinder with Grooves of Different Depths", *Journal of Visualization*, Vol. 8, 2005, pp. 295–303.

[15] C. Badalamenti, "On the Application of Rotating Cylinders to Micro Air Vehicles", PhD Thesis, City University London, UK, 2010.

[16] C. Badalamenti, and S. Prince, "The Effects of Endplates on a Rotating Cylinder in Crossflow" AIAA Paper 2008-7063. *AIAA Applied Aerodynamics Conference*, Hawaii, Aug. 2008.

[17] C. Badalamenti, C. and S. Prince, "Vortex shedding from a rotating circular cylinder at moderate sub-critical Reynolds numbers and high velocity ratio" Paper 2008-3.10.5, *26th International Congress of the Aeronautical Sciences*, 2008.

Contact Author Email Address

For information regarding this research, please contact: simon.prince@cranfield.ac.uk